UNIVERSITY OF LEEDS

This is a repository copy of *Discrete element modelling of the effect of aspect ratio on compaction and shear behaviour of aggregates*.

White Rose Research Online URL for this paper:
https://eprints.whiterose.ac.uk/201802/

Version: Accepted Version

Article:
Lu, R., Luo, Q., Wang, T. et al. (3 more authors) (2023) Discrete element modelling of the effect of aspect ratio on compaction and shear behaviour of aggregates. Computers and Geotechnics, 161. 105558. ISSN 0266-352X

https://doi.org/10.1016/j.compgeo.2023.105558

© 2023, Elsevier. This manuscript version is made available under the CC-BY-NC-ND 4.0 license http://creativecommons.org/licenses/by-nc-nd/4.0/.

Reuse
This article is distributed under the terms of the Creative Commons Attribution-NonCommercial-NoDerivs (CC BY-NC-ND) licence. This licence only allows you to download this work and share it with others as long as you credit the authors, but you can't change the article in any way or use it commercially. More information and the full terms of the licence here: https://creativecommons.org/licenses/

Takedown
If you consider content in White Rose Research Online to be in breach of UK law, please notify us by emailing eprints@whiterose.ac.uk including the URL of the record and the reason for the withdrawal request.

White Rose university consortium
Universities of Leeds, Sheffield & York

eprints@whiterose.ac.uk
https://eprints.whiterose.ac.uk/

Discrete element modelling of the effect of aspect ratio on compaction and shear behaviour of aggregatess

Rui Lu

School of Civil Engineering, Southwest Jiaotong University, Chengdu 610031, China

Email: lurui@my.swjtu.edu.cn

Qiang Luo

School of Civil Engineering, Southwest Jiaotong University, Chengdu 610031, China

MOE Key Laboratory of High-Speed Railway Engineering, Chengdu 610031, China

Email: lqrock@swjtu.edu.cn

Tengfei Wang*

School of Civil Engineering, Southwest Jiaotong University, Chengdu 610031, China

MOE Key Laboratory of High-Speed Railway Engineering, Chengdu 610031, China

ORCID: 0000-0003-4079-0687

Email: w@swjtu.edu.cn (*Corresponding author)

David P. Connolly

School of Civil Engineering, University of Leeds, Leeds LS2 9JT, UK

Email: D.Connolly@leeds.ac.uk

Kaiwen Liu

School of Civil Engineering, Southwest Jiaotong University, Chengdu 610031, China

MOE Key Laboratory of High-Speed Railway Engineering, Chengdu 610031, China

Email: kaiwen.liu@queensu.ca

Chunfa Zhao

State Key Laboratory of Traction Power, Southwest Jiaotong University, Chengdu 610031, China

Email: cfzhao@swjtu.edu.cn

Abstract

Coarse aggregates are essential for constructing railways and highways, as they affect structural performance through their compacted state and shear strength. Particle geometry influences these properties, but little research has quantitatively investigated how shape indexes impact mechanical indicators. This study addresses this gap by exploring the effect of particle aspect ratio on coarse aggregate compaction and shear behavior using the discrete element method (DEM). The study's key contribution is the development of novel equations that describe the correlation between packing porosity, inter-particle contact state, and aspect ratio control thresholds in a practical format. To do so, first, a point cloud database is compiled from laser scans of 700 natural aggregate particles. Each particle is classified using three aspect-ratio parameters: elongation, flatness, and flatness-elongation index (*FEI*). They are then digitized as rigid block particle models and compared against actual point clouds. Next, nine aggregates of representative shapes are assessed for their macro and mesoscopic mechanical responses using DEM-based vibro-compaction and direct shear tests. The compaction simulations indicate an exponential relationship between porosity and inter-particle coefficient of friction and show that aggregates with $FEI \approx 0.5$ are a good choice. The direct shear simulations consider the same initial porosity, and show that the relationship between peak shear strength and vertical stress follows a power function. Finally, the analysis of contact forces and fabric tensors implies that $FEI \approx 0.5$ may also facilitate particle fragmentation control.

Keywords: granular aggregates; aspect ratio; railway-highway; discrete element method; rigid block; laser scanning aggregates

1 Introduction

Coarse aggregates are used for a wide range of construction applications, including highway and railway sub-bases and rockfill dams (Xu and Wang, 2016; Xiao et al., 2020; Guo et al., 2022; Fu et al., 2022). Granular aggregates are usually irregular and form complex granular systems connected to surrounding fluid media and engineering structures (Mitchell and Soga, 2005; Cheng and Wang, 2018; Ngo and Indraratna, 2020). Researchers have demonstrated how the shape influences material behaviour in both laboratory and field investigations. There is extensive literature on this subject, such as packing density, shear strength, stiffness and permanent deformation (Shin and Santamarina, 2013; Cook et al., 2017; Lee et al., 2017; Payan et al., 2017). However, there is uncertainty in the conclusions drawn from the experimental study because natural or crushed mineral grains were employed, in which case variability exists in control variables and experimental results. To overcome this challenge, the discrete element method (DEM) has proven a valuable tool for analyzing the mechanical response of granular media (Cundall and Strack, 1979; Bono et al., 2014; Dai et al., 2016; Wu et al., 2021). Using it, grain morphology can be customized to reduce experimental complexity.

To maximise the resolution and contact detection efficiency in DEM modeling, a common assumption is that the granular particles can be approximated using discs and spheres (Cundall and Strack, 1979; Abbireddy and Clayton, 2010). However, their geometries can also be modelled using more complex shapes, including polygons (Fraige et al., 2008; Xiao and Tutumluer, 2017) and super-quadric geometries (Rothenburg and Bathurst, 1992; Lin and Ng, 1995; Zhao and Zhou, 2017). A shortcoming of these approximations is that as particle sizes increase (i.e. coarser aggregates), geometry simplifications reduce accuracy because particle shape has a dominant role on the behavior of the overall granular matrix. While these drawbacks are acknowledged, mathematical expressions are adequate for describing and generating complex particle shapes, such as the rotation-invariant spherical harmonic analysis (Garboczi, 2011; Zhou et al., 2015; Su and Yan, 2018) and Fourier mathematical method with random field theory (Bowman et al., 2001; Mollon and Zhao, 2014).

47 Optical microscopy, laser beam systems, and digital holography can also be used to obtain realistic
48 grain morphology (Zhang, 2017; Nie et al., 2021; Lu et al., 2022). Further, clump or rigid blocks (Itasca
49 Consulting Group, 2017) can be used in DEM approaches, with particle surface information used to
50 represent the actual aggregate shape.

51 Particle shape can be classified into three independent descriptors (Barrett, 1980; Cho et al., 2006):
52 form (such as aspect ratio and sphericity), angularity or roundness (Wadell, 1935), and roughness. The
53 packing fraction for form scale parameters has been estimated by (Donev et al., 2004; Ng, 2009), who
54 investigated the macro- and micro-behaviors of ellipsoids with varying aspect ratios. Meanwhile,
55 (Azéma and Radjaï, 2010) suggested an elongation parameter to distinguish between rounded-cap
56 rectangles in two dimensions before exploring the stress-strain behavior of these particles. To qualify
57 particle shape, sphericity (Cho et al., 2006; Zhang et al., 2020) has been used to study its correlation
58 with mechanical properties. The global shape parameters of aggregate assemblies remains the focus of
59 many works with regards to their influence on packing density, shear strength, and mesoscopic
60 characteristics (Fang et al., 2022; Kuhn et al., 2015; Zhao et al., 2020). Similarly, angularity has been
61 the subject of much attention due to its significant impact on particle mechanical properties (Lu et al.,
62 2022; Nie et al., 2020; Wu et al., 2021). However, it has been noted that the literature primarily focuses
63 on investigating shape effects while providing limited straightforward guidelines for engineering
64 practitioners.

65 Prior research in developing mathematical functions to explain the correlation between shape
66 indexes and mechanical parameters has been limited. Although aspect ratios remain prevalent in
67 engineering applications and technical guidelines, current specifications do not offer uniform values
68 for the limits of aspect ratios. For instance, ASTM (American Society of Testing and Materials, 2010)
69 suggests a long/medium aspect ratio of 2.0, medium/short aspect ratio of 3.0, and a ratio of 5.0 for fill
70 selection, while the Australian Standard (Australian Standard, 2007) recommends an optimal aspect
71 ratio of 2.0 and 3.0 for fill particles. Similarly, Chinese standards (National Railway Administration of

PRC, 2008, 2017) advocate a maximum to minimum axial dimension ratio of approximately 3:1. Using DEM, it may be plausible to optimize this ratio or generate more precise recommendations regarding the optimal shape indexes for specific mechanical performance.

In an attempt to study this relationship, this study uses a 3D DEM approach to investigate how aspect ratios affect coarse aggregates' packing characteristics and shear behavior. First, a laser scanner is employed to compile a point cloud database of 700 coarse aggregates. For each point cloud information, a rigid block unit is constructed using particle flow code. Based on the axial dimensions, elongation (*EI*), flatness (*FI*), and flatness-elongation index (*FEI*) are selected to quantify the aspect ratios of the point clouds and rigid blocks as a representation of the coarse aggregates. Then, a novel numerical protocol is used to simulate the aggregate compaction. Vibro-compaction creates a series of compaction levels by modifying the inter-particle coefficient of friction. Following this, numerical direct shear tests are performed to map aspect ratios with vertical pressure and shear strength. A mesoscopic perspective is gained by examining the contact forces and fabric tensor between particles. Finally, based on the particle aspect ratios, approaches to control compaction quality and prevent particle fragmentation are discussed.

2 Methods

2.1 Shape characterization

Aspect ratio is commonly measured using three orthogonal axial dimensions ($P_1 > P_2 > P_3$), calculated using principal component analysis (Zhou and Wang, 2017). Two orthogonal surfaces of a particle are used to calculate the elongation and flatness indices based on three axial dimensions. (Zingg, 1935; Zhao and Wang, 2016), expressed by:

$$EI = \frac{P_2}{P_1} \tag{1}$$

$$FI = \frac{P_3}{P_2} \tag{2}$$

where EI is the elongation index ranging from 0 to 1, and *FI* is the flatness index ranging from 0 to 1. A particle becomes more prolate when *EI* approaches 0, while the particle becomes more oblate when its *FI* approaches 0.

The shape indexes *EI* and *FI* help measure particle shape irregularity in three dimensions. To visualize the combined effect of particle shape and to facilitate subsequent analysis, the flatness-elongation index (*FEI*) (Rajan and Singh, 2017) is also chosen for quantification, with the aim of establishing a relationship between it and both compaction and shearing properties indicators. The definition of *FEI* is given as:

$$FEI = EI \cdot FI = \frac{P_3}{P_1} \tag{3}$$

where *FEI* ranges from 0 to 1. Particles with a high maximum orthogonal axial dimension compared to their minimum dimension result in a lower *FEI* value ($FEI \rightarrow 0$), and thus are more irregular in shape. Alternatively, particles with a maximum orthogonal axial dimension are only slightly larger in comparison with their minimum dimension, resulting in a higher *FEI* value ($FEI \rightarrow 1$). These particles are more spherical in shape.

2.2 Particle geometry modelling

First, 3D laser scanning technology was used to obtain the natural shape characteristics of the coarse aggregates (see Fig. 2). In DEM simulations, clumps often serve as non-spherical particle models. These are formed by fusing two or more spherical units or 'pebbles' (Ferellec and McDowell, 2010; Li et al., 2015). The surface of a clump is defined by the position and radius of each constituting pebble. The closer the number of pebbles is to infinity, the more the clump shape approximates natural particles, resulting in a trade-off between precision and computational efficiency. As an alternative to the clump concept, rigid block models (Rblocks) within the DEM framework (Itasca Consulting Group, 2017) simulate actual particles without the use of spheres. By employing scanned point clouds, an Rblock mirrors a convex polyhedron, comprised of triangular facets. Literature (Lu et al., 2022)

supports the Rblocks' ability to robustly and effectively characterize irregular surfaces while retaining computational efficiency. A comprehensive analysis of this is forthcoming in Section 3. The Gilbert–Johnson–Keerthi (GJK) algorithm (Gilbert et al., 1988) offers a potential avenue for maximizing computational efficiency in contact detection and resolution by utilizing a single contact between two convex objects. Figure 1 illustrates an iterative approach using the Minkowski difference to determine convex shape overlap. The Minkowski difference of two convex sets in mathematics refers to the set of pairwise differences between all points from the two sets. This mathematical concept facilitates a straightforward determination of contact between two particles: if the Minkowski difference contains the origin, the two particles are in contact. The entire process can be expressed as:

$$m(A,B) = \{x - y; x \in A, y \in B\} \tag{4}$$

$$d(A,B) = |min\, m(A,B)| \tag{5}$$

where $m(A,B)$ denotes the Minkowski difference, *x* and *y* are any of the two points on A and B, and $d(A,B)$ denotes the distance between convex polyhedral *A* and *B*.

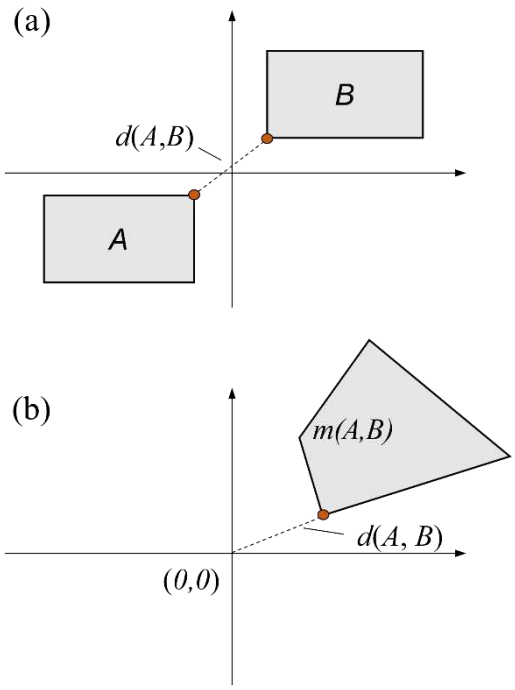

Fig. 1. Schematic of GJK algorithm for Rblocks contact: (a) the distance between convex *A* and *B* in a real coordinate system; (b) Minkowski difference of two convex sets (*A* and *B*) and its distance to

the origin.

This study focuses on coarse, cohesionless grains (aggregates), and thus interparticle adhesion is not considered. To represent interactions between particles, a linear-based contact model is used, which uses linear springs acting in parallel. Linear springs at the contact location provide the particles' linear elastic (tensionless) frictional properties (Cundall and Strack, 1979).

3 Materials and shape characterization

3.1 Reconstruction of realistic aggregate

The particles under study were coarse aggregates sampled from an in-situ subgrade fill on a high-speed rail line in the Sichuan Province of China. These aggregates typically have a particle size range of 2.36 to 31.5 mm. The particle size range was divided into seven groups to ensure each group's minimum to maximum particle size ratio exceeded 0.50. One hundred particles were selected from the respective groups, totaling 700 coarse aggregate particles. The acquisition of genuine 3D morphology from the samples was accomplished using a Range7 laser scanner (Figure 2), manufactured by Konica Minolta Inc.

The scanning procedure (Figure 2) was as follows:

a) To ensure precise measurements, the scanner was stationary on a stable surface, firmly secured by a tripod to minimize vibrations. The particles under investigation were arranged on a revolving platform. The internal environment was carefully controlled and maintained within specified parameters (10 to 40 °C, 65% relative humidity or lower) compatible with the equipment's operation.

b) The optical lens served as a focal point, measuring the particles at a distance of 450 to 800 mm. Subsequently, lasers enabled the acquisition of the point clouds on the surface of the particles. The device had a scanning accuracy of approximately ± 40 μm, sufficient for describing the morphological traits of the particles.

c) Controlling the rate of particle rotation involved the use of a fixed stepping angle of 60°, determined by the size of the particle and the scanner's precision. The scanner captured the upper

portion of the particle at a full angle before inverting it to align the unscanned region with the scanner for rescanning. The upper- and lower-point clouds were combined and aligned to create a high-fidelity representation of the particle's surface. Through this process, point clouds and correlated DEM Rblocks were generated, ensuring accuracy in the description of the coarse aggregates.

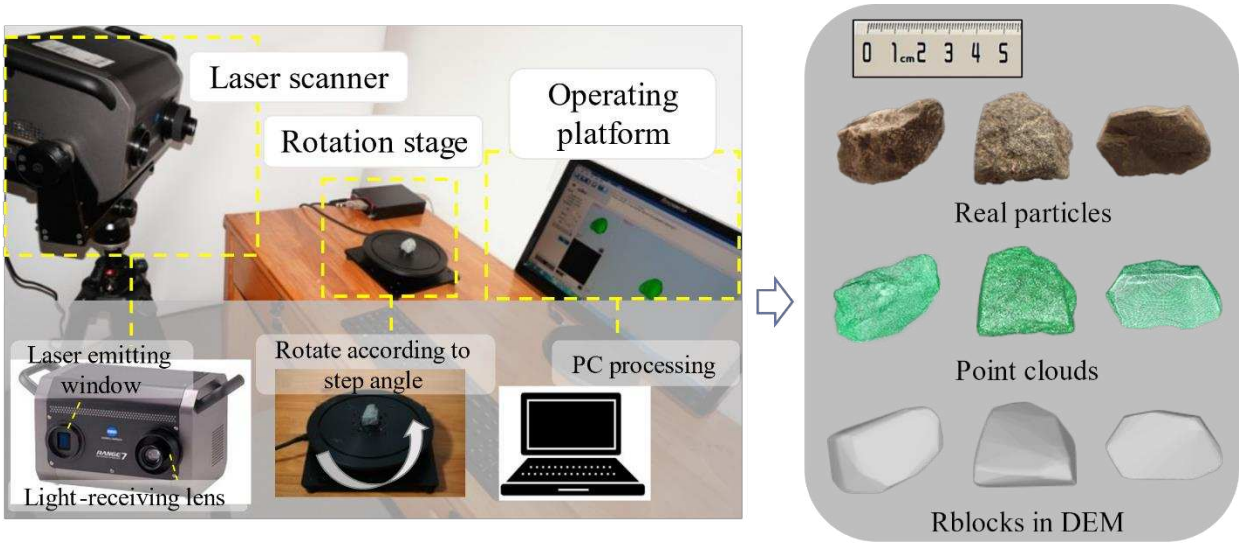

Fig. 2. 3D laser scanning system and an illustration of real coarse aggregates, point clouds, and Rblocks.

3.2 Statistical analysis of shape indexes

Previous studies have demonstrated the significance of shape indices for describing granular materials (Xiao et al., 2020; Zhao and Wang, 2016). These statistical shape indicators offer an extensive understanding of the coarse aggregates' shape characteristics, which aid in the selection of representative particle samples for analysis. Figure 3 depicts the frequency distribution histogram of the calculated *EI* and *FI* for 700 coarse aggregates, comprising both real particles and Rblocks. The aspect ratio distribution was in close proximity to the Weibull distribution, as indicated by the histogram. Hence, a fitting method was used to determine the corresponding curvature of the probability density distribution function. The resulting function is expressed as follows:

$$f(x;a,b)=\begin{cases}\frac{k}{\lambda}\left(\frac{x}{\lambda}\right)^{k-1}e^{-\left(\frac{x}{\lambda}\right)^{k}} & x\geq 0\\ 0 & x<0\end{cases} \tag{6}$$

where x denotes the *EI* or *FI*, k is the shape parameter, and λ is the scale parameter.

Table 1 showcases the fitted λ and k values, along with statistical indicators such as mean, coefficient of variation (C_v), skewness (*SK*), and kurtosis (*KU*), derived from the data in Figure 3. The results suggest that the Rblocks closely resemble the aspect ratio characteristics of the natural aggregates. Thus, it can be inferred that Rblocks preserve the natural aggregates' aspect ratio features.

According to (Lu et al., 2022), particle angularity can be more accurately represented using Wadell's roundness of Rblocks when the number of facets (which is the unit of Rblocks) is approximately 300. Thus, Rblocks were set to 300 to ensure the simulation's realism. Roundness was initially delineated by Wadell (1935) as the ratio between the radius of a particle projection's corner portion and the maximum radius of its inscribed circle. Methods to automate Wadell's roundness evaluation process efficiently through digital image processing have been proposed (Nie et al., 2020; Zhao and Wang, 2016; Zheng and Hryciw, 2016). Further details on angular scale are available in the aforementioned literature.

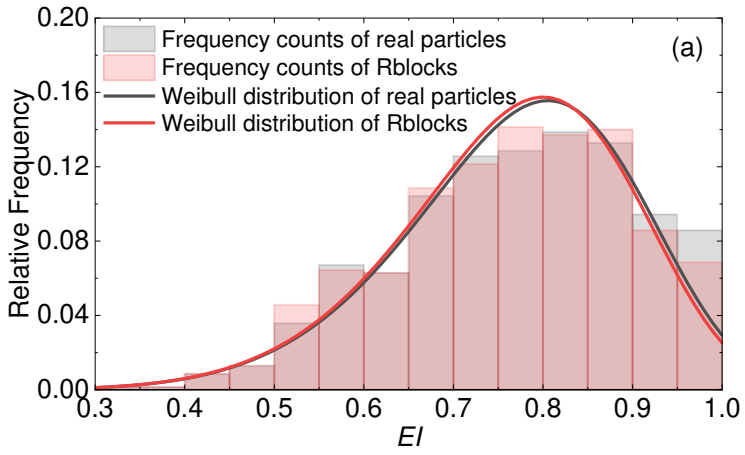

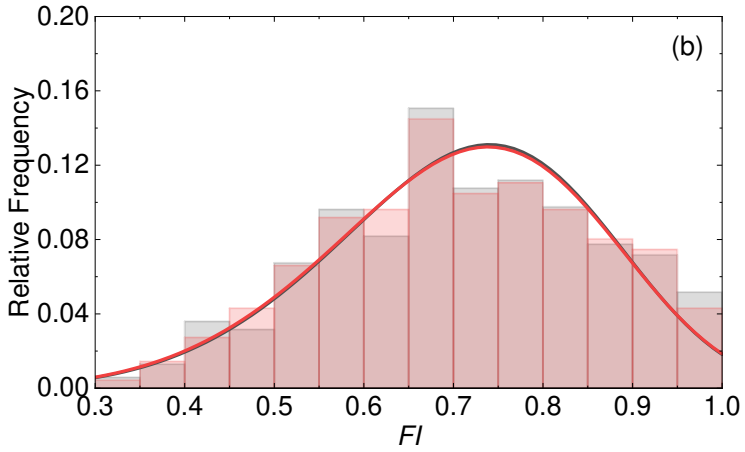

Fig. 3. Frequency histograms of *EI* and *FI* and the fitted Weibull distributions: (a) real particles; (b) Rblock model.

Table 1. Fitted parameters under Weibull distribution and statistical indicators of aspect ratios.

	EI		*FI*	
	Real particles	Rblocks	Real particles	Rblocks
Mean	0.769	0.764	0.708	0.707
C_v	0.173	0.172	0.215	0.216
SK	−0.383	−0.391	−0.212	−0.183
KU	−0.485	−0.420	−0.507	−0.465
k	6.984	6.393	5.319	5.380
λ	0.824	0.819	0.768	0.769

3.3 Particle sample selection

According to Zingg (1935), the *EI* and *FI* of coarse aggregates can be divided into three groups: prolate, oblate, and scalene. Following the known *EI* and *FI* values ranges, nine representative particle samples were selected at *EI*s of approximately 0.95, 0.75, and 0.55, and *FI*s of approximately 0.95, 0.75, and 0.55. DEM simulations were then used to analyze these samples, which are illustrated in Figure 4. As *EI* decreases, the particle prolate becomes more pronounced; as *FI* decreases, the particle oblate becomes more apparent. There is a greater degree of scalene when the values of *EI* and *FI* are both small, meaning that there is a significant difference between the three axial dimensions (P_1, P_2 and P_3) of a particle.

The DEM specimens corresponding to these nine Rblocks are named according to their shape characteristics. As shown in Fig. 4.

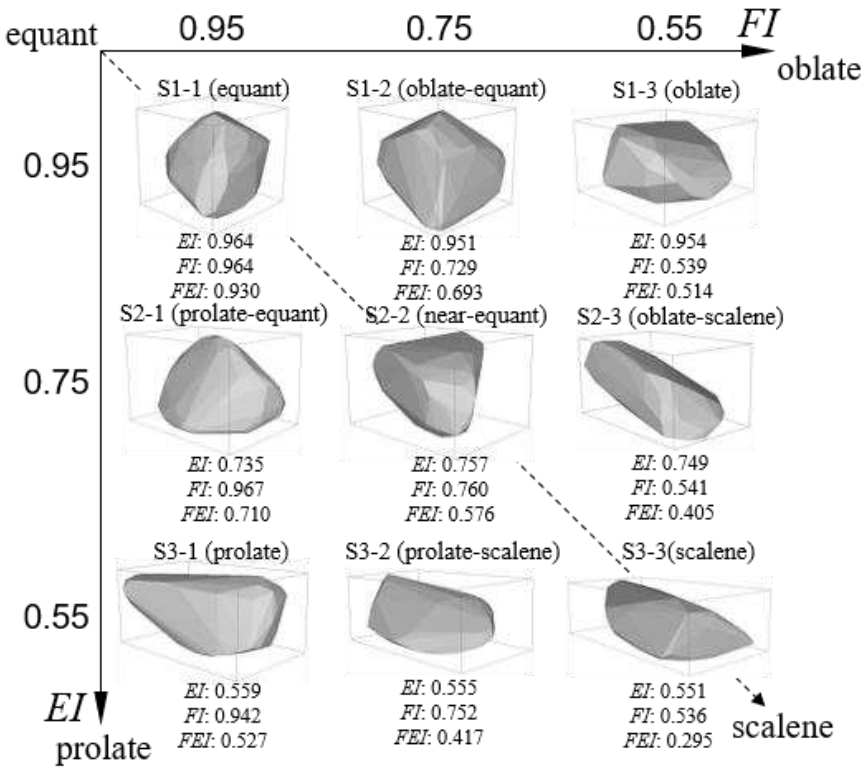

Fig. 4. Particle shape classification using Zingg's bivariate method (Zingg, 1935).

4 Models and calibration

4.1 Vibro-compaction model

Using gravitational deposition and additional compression, the inter-particle friction coefficient μ_p is usually set to zero in DEM to achieve dense specimens (Abbireddy and Clayton, 2010; Gong et al., 2019; Nie et al., 2021). According to this method, a larger value of μ_p means the particles are less likely to slide between one another. A smaller μ_p means particle sliding is easier, and thus particle rearrangement happens more easily under external forces, resulting in a denser aggregate.

Compaction simulations were performed for each of the nine typical Rblocks. A variety of packing densities were obtained based on the initial values of $\mu_p = 0, 0.1, \cdots, 1$. Since vibro-compaction is a dynamic process, the DEM simulation employed a blend of viscous and local damping (refer to Table 2). The damping coefficients employed in the numerical model were calibrated as per the findings of (Zhou and Sun, 2013). Other DEM contact parameters were set based on the calibration results

described in Section 4.3. Compression was achieved using surface vibration compaction (Figure 5), via the following steps:

a) The randomly generated Rblocks were placed in a cuboidal domain with a length, width, and layer thickness of 150 mm. The equivalent particle size of the Rblocks was 20 mm.

b) A rigid load plate compacted the specimen after the Rblocks had been subjected to gravitational deposition and reached stability. The vibration frequency was 50 Hz , cycling the force between 2.88 kN (18 kPa), and 52.88 kN (330.5 kPa) (National Railway Administration of PRC, 2010). The compaction process was considered complete after the porosity of each specimen reached stability.

c) Steps a and b were repeated three times, and particles above 350 mm in height removed. Note that the final specimens had the exact dimensions as the direct shear box in the physical tests (Zhang, 2017).

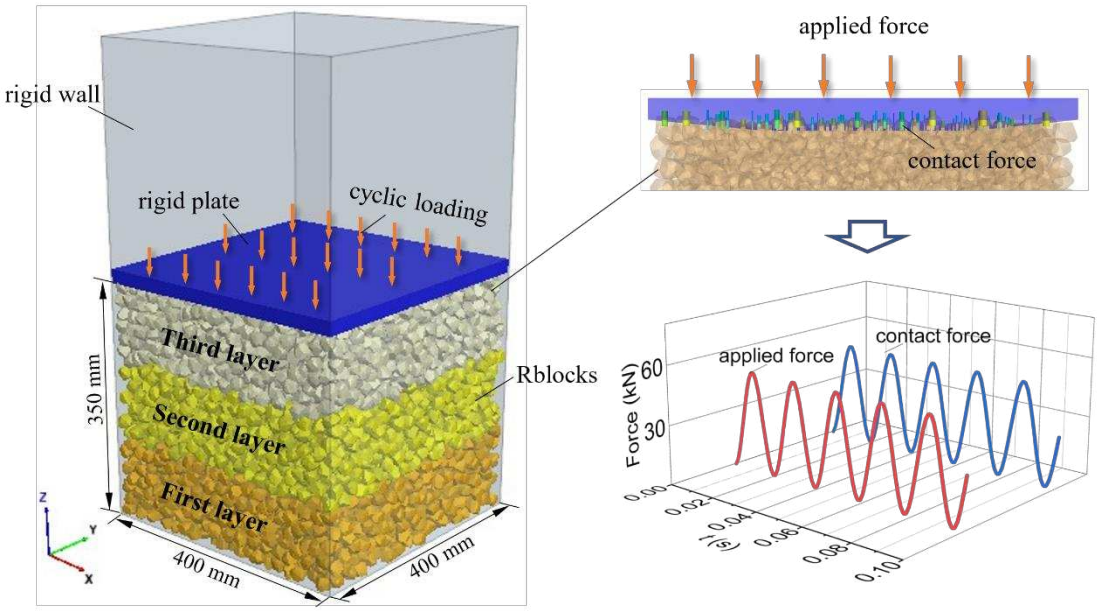

Fig. 5. Schematic of the surface vibratory compaction method for achieving target packing density of coarse aggregates: the applied force on the specimen from the rigid plate was equal to and synchronized with the contact force received by Rblocks.

4.2 Direct shear test on compacted samples

Direct shear simulations were also performed for homogenous particle matrices consisting of each of the nine Rblock types. Note that the vertical stresses σ_n applied to each specimen are 20, 50, 100,

and 150 kPa. Using the calibration results in Section 4.3, the other DEM contact parameters were be set. As noted in Section 6.1, the initial condition of each specimen was determined through compaction simulation, but the corresponding packing density remained unchanged.

The shear strength of the coarse aggregates was investigated using direct shear tests. Similar to the container for the post-compaction specimens, the dimensions of the direct shear device in the numerical test were 400×400×350 mm, with a 5 mm shear gap in the middle (Figure 6). During the shear process, the upper part of the shear box was fixed, and the lower part was sheared along the horizontal direction at a specific rate. The upper and lower walls maintained the load applied to the specimens until the shear displacement reached 80 mm (20% of the length of the shear box), at which point the test was terminated. Figure 6 illustrates the final state of the compacted aggregates in shear.

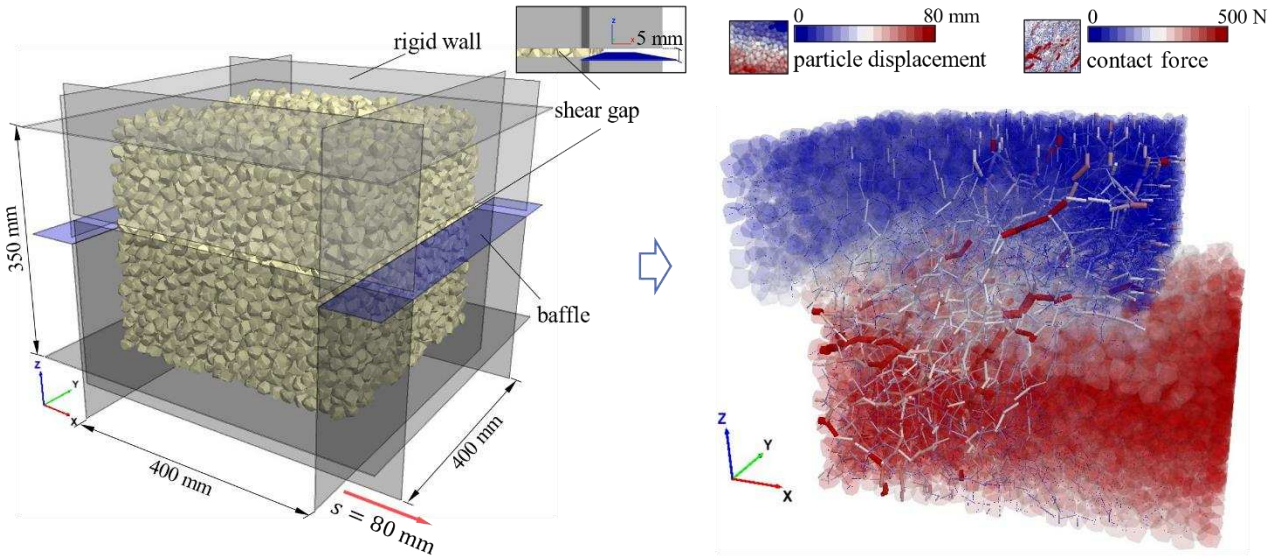

Fig. 6. Schematic of DEM simulations for the direct shear test: baffle prevents particles from spilling out during the shearing process.

4.3 Parameter calibration

The DEM parameters were calibrated by comparing them with experimental data (Zhang, 2017). The experimental setup for direct shear is illustrated in Figure 7. The shear box had a volume of 400 mm×400 mm×350 mm and housing coarse aggregates with porosity of 0.4. The tests utilized

maximum hydraulic actuator loads of 300 kN and 100 kN in the vertical and horizontal directions, respectively.

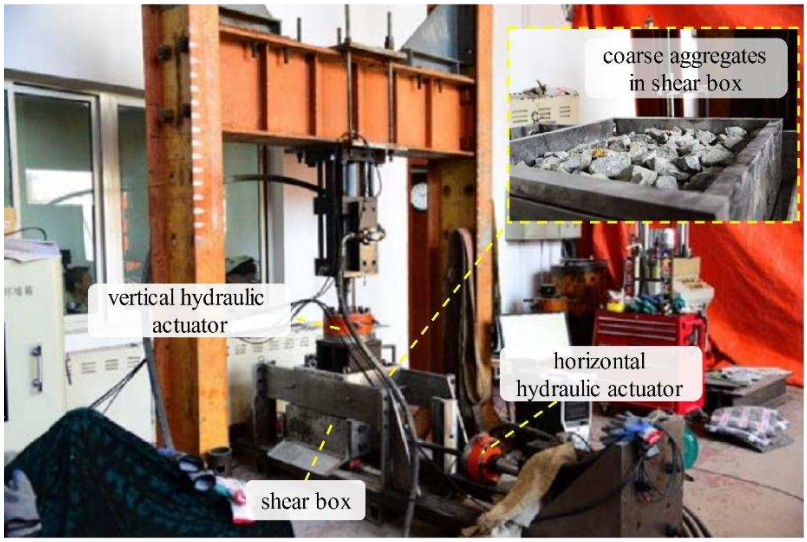

Fig. 7. Overview of the direct shear testing system (Zhang, 2017).

Note that the particles employed in the study by Zhang (2017) were sourced differently from the scanned particles currently under scrutiny. Despite this, several compelling reasons justify the use of these experiments for calibration. Predominantly, both aggregates - frequently applied in railway construction - originate from crushed rocks with similar strengths and shapes. Additionally, the direct shear device featured in the numerical experiments aligns with the methodology documented in the experimental study. The preparation of the numerical specimen was executed as follows: first, non-overlapping balls were generated within a shear box of predetermined porosity, and the three-dimensional coordinates and volumes of each ball were calculated. The porosity and gradation of the balls were kept consistent with literature (Zhang, 2017). Second, the balls were removed and Rblocks of coarse aggregate were generated at the original coordinates of each ball, with equal volumes and random angles. The particle shape profile used for each Rblock was randomly selected from the scanned 700 coarse particles. Lastly, the final state was determined by conducting sufficient time steps to ensure a stable equilibrium between the Rblocks.

As described in Section 2.2, there was no adhesion between the coarse aggregates meaning a linear

contact model was a suitable assumption. Combining the mesoscopic parameters related to the direct shear tests (Bian et al., 2015; Xiao and Tutumluer, 2017; Zhang, 2017) and the experimental data (Zhang, 2017), the calibration results and the microscopic parameters are presented in Table 2 and Figure 8.

Table 2. The DEM parameters of the direct shear simulation after calibration.

	Micro-parameters	Unit	Value
	Normal stiffness of particle	MN/m	20
	Tangential stiffness of particle	MN/m	10
	Normal stiffness of wall	MN/m	100
	Tangential stiffness of wall	MN/m	100
	Wall–particle frictional coefficient	/	0.40
Vibro-compaction	Interparticle frictional coefficient	/	0, 0.1 ⋯, 1.0
	Local damping	/	0.05
	Normal viscous damping	/	0.20
	Tangential viscous damping	/	0.20
Direct shear	Interparticle frictional coefficient	/	0.60
	Local damping	/	0.7

Note: As the direct shear test is a quasi-static process, local damping of 0.7 is used for the contact.

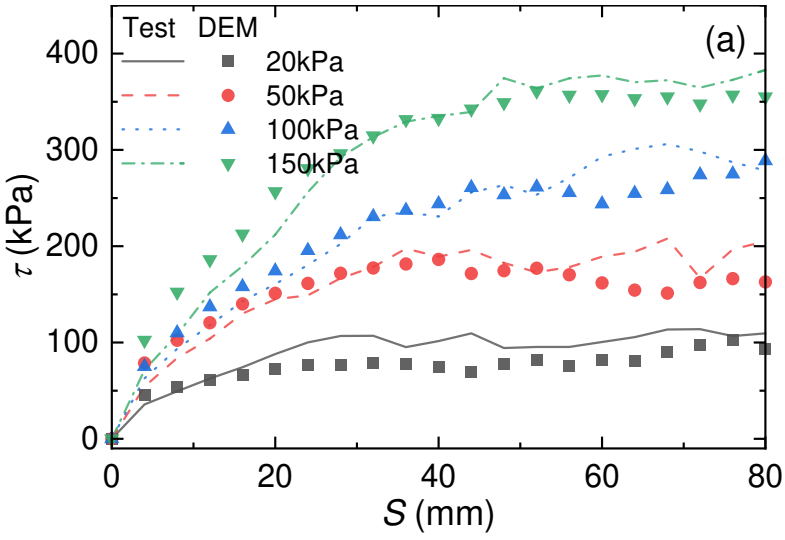

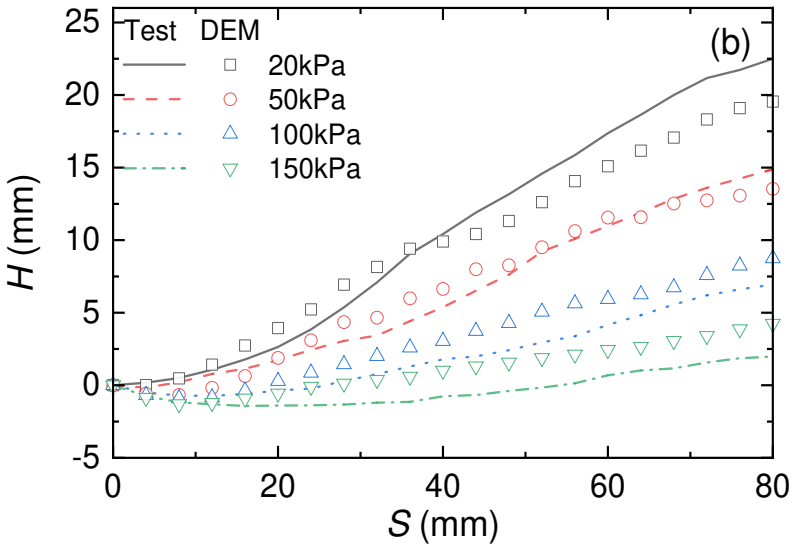

Fig. 8. DEM calibration results compared to (Zhang, 2017): (a) shear strength; (b) vertical displacement (τ is the shear strength, H is the vertical displacement, and S is the shear displacement).

5 Analysis of compaction characteristics

5.1 Effect of particle shape on porosity

The final compacted state of each specimen was measured using measuring spheres (Itasca Consulting Group, 2017) for porosity determination. The measuring sphere reflects the percentage of void volume within the sphere, meaning it reflects the porosity of a region inside it. Figure 9 shows the porosity of nine specimens after compaction for a series of μ_p values ($\mu_p = 0, 0.1, \cdots 1.0$). The porosity of the specimens increases with increasing μ_p within the same sample, but the rate slows when approaching $\mu_p = 1$. All particle aspect ratios exhibit the same pattern, which is similar to that observed in particle porosity with inter-particle friction coefficient (Abbireddy and Clayton, 2010; Huang et al., 2015). The relationship between porosity n_p and μ_p of specimens with different particle aspect ratios can be fitted using an exponential function:

$$n_p = \zeta - \alpha_1 \cdot \alpha_2{}^{\mu_p} \tag{7}$$

where ζ, α_1 and α_2 denote the regression coefficients respectively, as shown in Table 3.

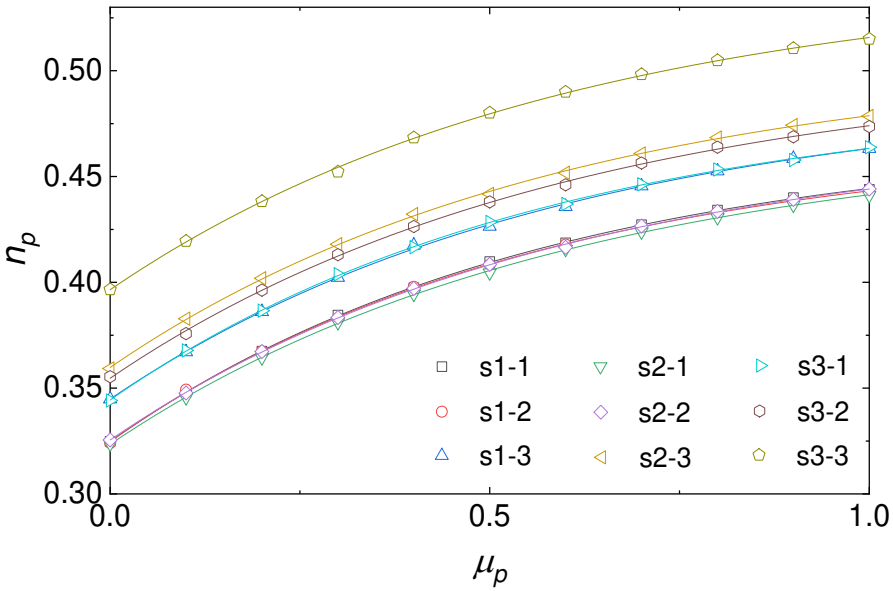

Fig. 9. Variation on the porosity of specimens under different shapes and different interparticle-friction coefficients.

Table 3 shows that the curve fit is more sensitive to ζ compare to α_1 and α_2. For example, considering all samples, the range of $\Delta\zeta$ is 0.07, while for $\Delta(\alpha_1 \cdot {\alpha_2}^{f_p})$ the range is 0.005. This is because ζ is primarily affected by the particle aspect ratio, while α_1 and α_2 are related to the gradient of the fitted curve which is similar for all particles. Therefore, in the subsequent analysis, α_1 and α_2 are set as constants, with values 0.145 and 0.18, respectively.

Table 3. The corresponding regression coefficient data after the fitting of Eq. (4).

ID	ζ	α_1	α_2	R^2
S1-1	0.469	0.144	0.171	99.35%
S1-2	0.468	0.143	0.171	99.52%
S1-3	0.491	0.146	0.189	99.51%
S2-1	0.469	0.146	0.190	98.99%
S2-2	0.471	0.146	0.187	99.66%
S2-3	0.506	0.146	0.185	99.19%
S3-1	0.488	0.144	0.174	99.73%
S3-2	0.502	0.148	0.191	99.19%
S3-3	0.543	0.147	0.189	99.86%

Note: R^2, Goodness of fitting.

Next, a function for correlating the shape parameters EI, FI and ζ was constructed. As show

in Figure 10a, the relationship between EI, FI, and ζ satisfies the quadratic equation (refer to Eq. (8)). Concerning Eq. (7), n_p can be derived using Eq. (9). In particular, when $EI = 0.869$ and $FI = 0.839$, there exists a minimum value, $\zeta_{\min} = 0.472$.

$$\zeta(EI, FI) = 1.09 - 0.68EI - 0.77FI + 0.29EI^2 + 0.35FI^2 + 0.21EI \cdot FI \quad (8)$$

$$n_p = \zeta(EI, FI) - \alpha_1 \cdot {\alpha_2}^{\mu_p} \quad (9)$$

To corroborate the aforementioned calculations, the published work (Donev et al., 2004) was examined. In their study, a modified Lubachevsky-Stillinger algorithm was utilized to estimate the packing fraction of randomly jammed frictionless hard ellipsoids in three dimensions. The algorithm, which incorporated controlled particle growth, is an event-driven molecular dynamics simulation (Donev et al., 2005a, 2005b). The packing fraction of ellipsoids with three orthogonal axial dimensions α: 1: 1 (prolate for $\alpha > 1$, oblate for $\alpha < 1$) and α: 1: α^{-1} (aspherical) as a function of α was determined. It was found that the n_p of ellipsoidal aggregates decreased and then increased with increasing *FEI*, with the densest state ($n_p \approx 0.29$) for prolate and oblate ellipsoidal particles at a *FEI* of 0.67 and the densest state ($n_p \approx 0.265$) for aspherical ellipsoidal particles at a *FEI* of 0.64. Similarly, for coarse aggregates, n_p decreased and then increased with increasing *FEI*, reaching the densest state ($n_p \approx 0.326$) at an *FEI* of approximately 0.72 (*EI* = 0.869 and *FI* = 0.839), as determined by Eq. (9) when $n_p = 0$ (Figure 10b). This was attributed to the increase in the number of contacts resulting from the additional degrees of freedom of the ellipsoids. The denser packing of the particles was a consequence of the need for more contacts per particle to eliminate all local and collective degrees of freedom. However, the increase in porosity for large *FEI* was due to exclusion volume effects. It is worth noting that the results for coarse aggregates differ somewhat from the literature (Donev et al., 2004) due to the Rblocks model's ability to characterize the angularity of the particles. (Cho et al., 2006) concluded that as the particle roundness decreases (angularity increases), the corresponding void ratio also increases. Furthermore, standard balls were compacted under identical conditions, yielding an n_p of

approximately 0.36, which is identical to the reported results (Donev et al., 2004).

Regarding porosity, Figure 10b shows that EI and FI have approximately equal influence. For instance, the n_p value for an oblate-equant specimen ($EI = 0.95, FI = 0.75$) is 0.330 and for a prolate-equant specimen ($EI = 0.75, FI = 0.95$) is 0.332, equating to a 0.6% difference. Similarly, n_p for an oblate specimen ($EI = 0.95, FI = 0.55$) is 0.352 and for a prolate specimen ($EI = 0.55, FI = 0.95$) is 0.353 equating to a 0.28% difference; As is evident from the above cases, the effect of EI and FI on n_p of the coarse aggregates is approximately the same. The intermediate axis (P_2) of a particle exerts a minimal influence on n_p, meaning that the contribution of P_2 can be ignored.

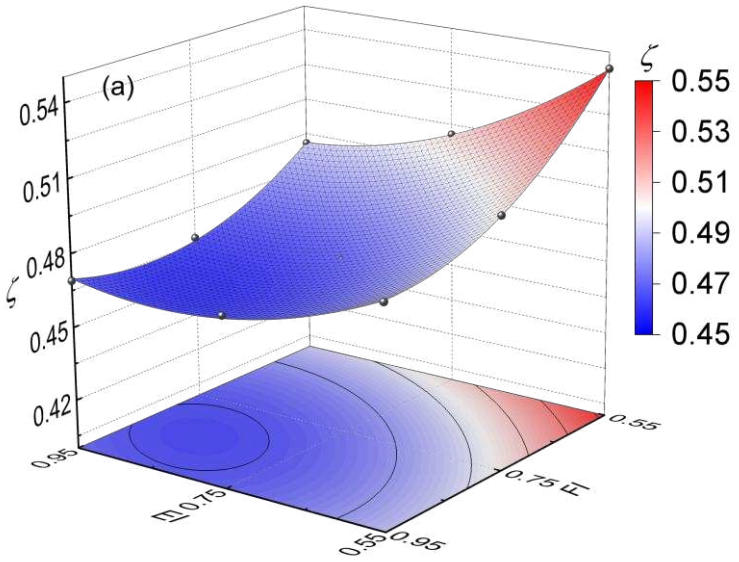

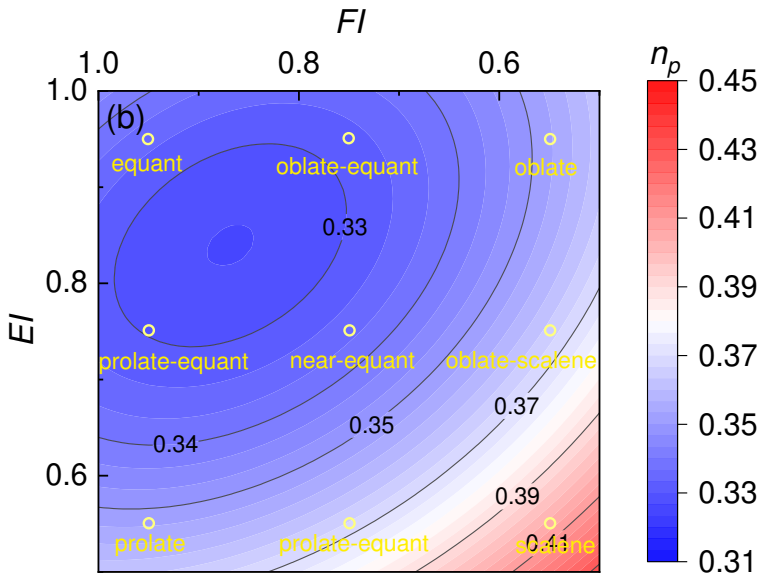

Fig. 10. Regression coefficients ζ and porosity n_p as a function of EI and FI: (a) ζ; (b) n_p when $\mu_p = 0$.

5.2 Compaction control

Compaction performance refers to the ability of a body of coarse aggregate to achieve a desired level of compaction under external pressure. Particles with irregular shapes are more likely to form interlocking that prevents effective compaction. According to (American Society of Testing and Materials, 2010; Australian Standard, 2007; National Railway Administration of PRC, 2008, 2017), the maximum and minimum axial dimensions of coarse particles used as ballast or subgrade fill are explicitly limited. The most rigorous requirement is that they conform to an aspect ratio of 3.0. Since the ratio limits are still based on engineering experience, it remains to be seen whether there is a clear threshold between the variation in particle aspect ratios and the compaction properties. Although the analyses in this study are discussed for samples with different particle shapes at homogeneous particle sizes, the method allows the particle shape to be controlled as a single variable, thus providing a better understanding of the influence of particle shape on compaction.

Therefore, this section explores how to control the compaction of coarse aggregates by studying the influence of FEI. Based on n_p of specimens with differing aspect ratios, the relative porosity P_r is defined as:

$$P_r = \frac{n_{p\,max} - n_p}{n_{p\,max} - n_{p\,min}} \tag{10}$$

where $n_{\mathrm{p\,max}}$ is the value for the scalene specimen ($EI = 0.55$, $FI = 0.55$), which is close to the aspect ratio limit requirement of coarse aggregates. $n_{\mathrm{p\,min}}$ is the minimum value computed using Eq. (9). Note that μ_p when determining the values of $n_{\mathrm{p\,min}}$ and $n_{\mathrm{p\,max}}$, μ_p is 0.6.

Fig. 11 shows the exponential relationship between P_{r} and FEI for μ_p=0.6, as described in Eq. (11). To maximise the fit, 16 additional particles within the range: 0.55 < EI < 0.95, 0.55 < FI < 0.95, were selected for calculation under the same conditions, supplementing the existing calculation results for the above representative particles. As FEI increases, P_{r} first increases rapidly and then gradually. The maximum curvature of this function curve is indicated as the threshold point for the variation of P_{r} with FEI. The maximum value of curvature occurs when $FEI = 0.469$.

$$P_{\mathrm{r}} = 0.97 - 21.76e^{-10FEI} \tag{11}$$

The results suggest that coarse aggregates were difficult to compact when there was significant axial particle size difference, particularly if the aggregates had prolate, oblate, or scalene shapes. It is possible to control the packing density by keeping *FEI* greater than the threshold (0.469). Accordingly, the maximum and minimum axial dimensions ratio is approximately 2:1.

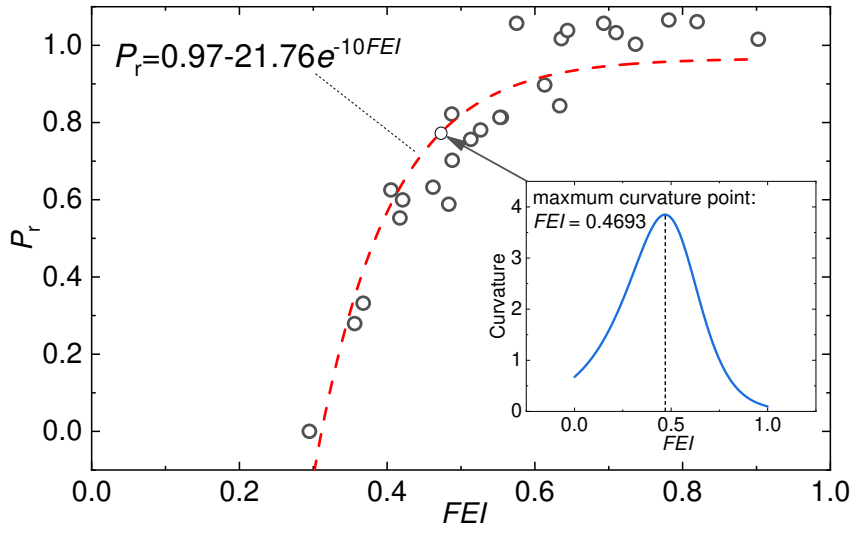

Fig. 11. Variation in n_p with *FEI* and the corresponding curvature value distribution at $\mu_p = 0.6$.

6 Analysis of shear behaviour

6.1 Shape effects on shear strength

Nine aggregate mixes formed from the aforementioned shapes were analyzed under controlled initial porosity conditions, with the aim of investigating the effect of aspect ratio on shear behavior. Following the above analysis, $n_p = 0.42$ was selected as the final compaction criterion. The preset friction coefficient μ_p was calculated using Eq. (9) to perform compaction on specimens. Table 4 shows the preset friction coefficient μ_p and porosity n_p for each specimen. All n_p values were close to 0.42, with a maximum difference of 0.65%.

Table 4. μ_p and n_p values derived from Eq. (4) and DEM simulations.

	μ_p	n_p	Relative error
S1-1	0.614	0.418	−0.57%
S1-2	0.626	0.419	−0.21%
S1-3	0.431	0.421	0.12%
S2-1	0.647	0.417	−0.62%
S2-2	0.627	0.418	−0.48%
S2-3	0.339	0.423	0.65%
S3-1	0.423	0.418	−0.38%
S3-2	0.367	0.422	0.49%
S3-3	0.142	0.421	0.17%

Figures 12 (a) - (i) illustrate the variation of shear strength τ and vertical displacement H of each specimen under the direct shear test conditions. The data indicates τ for each specimen exhibited strain-hardening, whereas H primarily showed a trend of small shear contraction followed by continuous shear expansion. Further, the specimens with different aspect ratios showed an increase in shear strength and vertical displacement with the decrease of EI and FI.

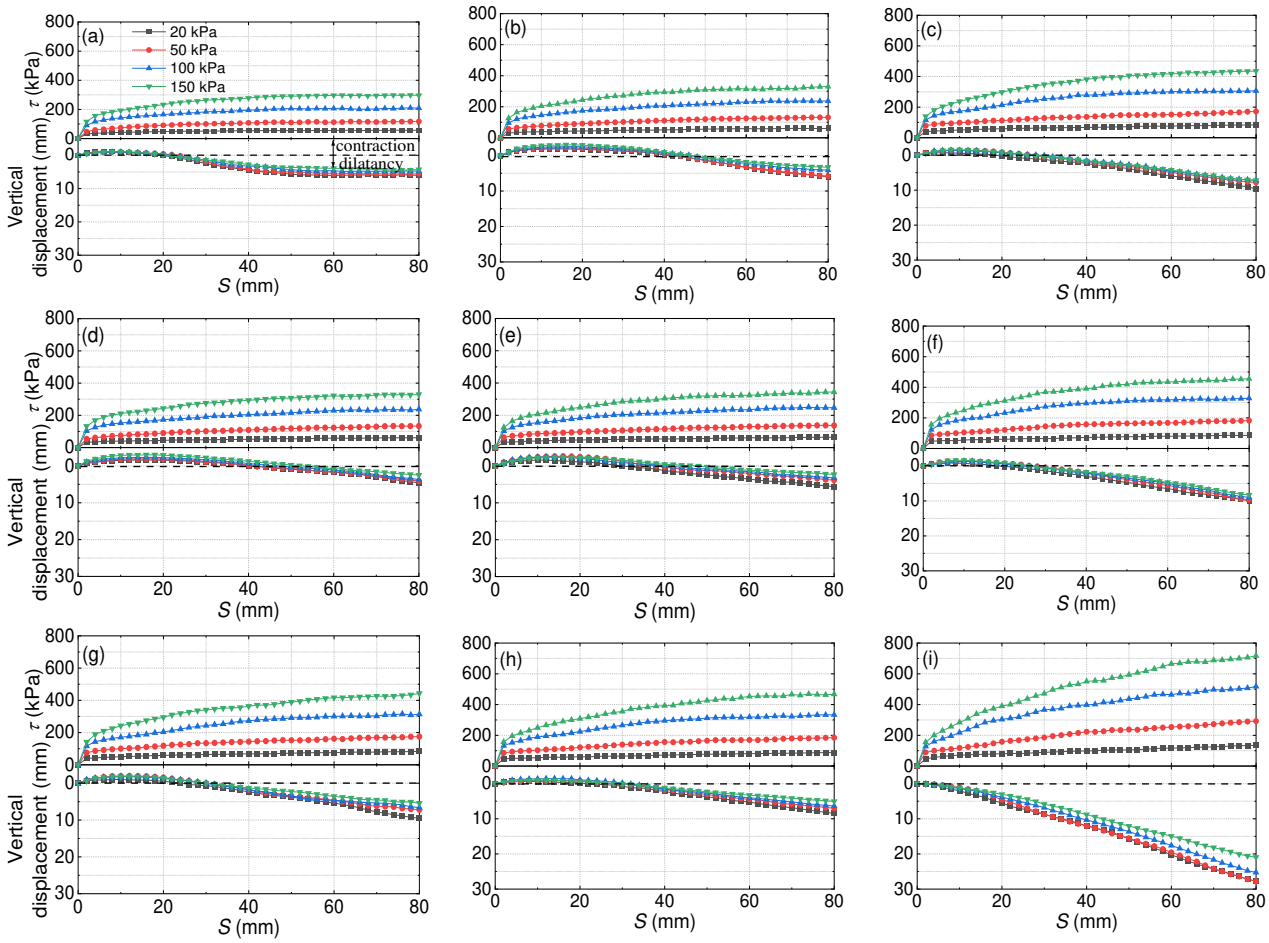

Fig. 12. Shear strength and vertical displacement of the specimens in direct shear simulations under the same porosity: (a) S1-1; (b) S1-2; (c) S1-3; (d) S2-1; (e) S2-2; (f) S2-3; (g) S3-1; (h) S3-2; (i) S3-3.

As shown in Fig. 13, the peak shear strength τ_p and the vertical stress σ_n had a non-linear relationship. A power function relationship was used to describe shear strength envelope of each specimen:

$$\tau_{\mathrm{f}} = \eta \sigma_n{}^{\beta} \tag{12}$$

where η, β denote the regression coefficients, as specified in Table 5.

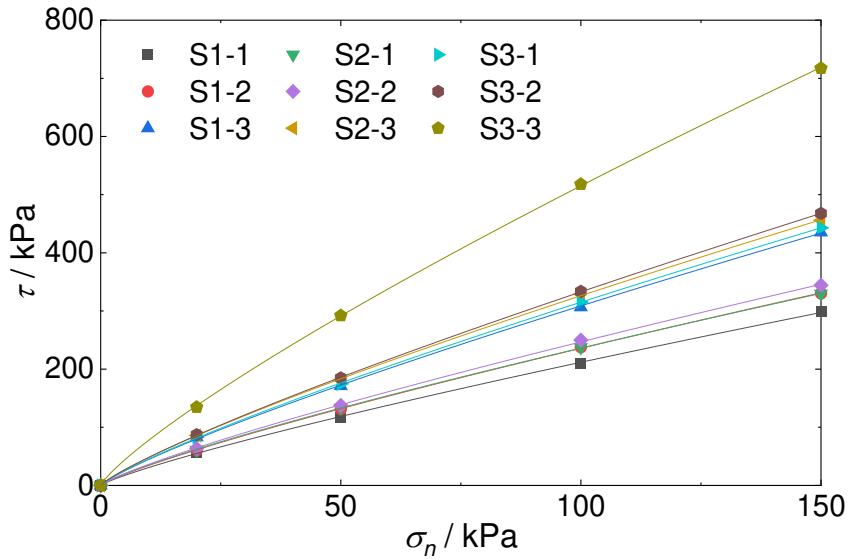

Fig. 13. Shear strength envelopes for specimens of different shapes.

Table 5 shows that the value of $\Delta\eta$ varied by 7.23 across all simulations while $\Delta\beta$ varied by 0.018. This is because the regression parameter η was mainly affected by particle shape, while β was relatively constant. Therefore, a typical value of β=0.83 was assumed to be representative for all samples.

Table 5. The regression coefficients for the fitting of Eq. (12).

ID	η	β	R^2
S1-1	4.48	0.838	99.98%
S1-2	4.99	0.837	99.99%
S1-3	6.46	0.840	99.98%
S2-1	5.25	0.827	99.99%
S2-2	5.36	0.832	99.97%
S2-3	7.12	0.831	99.98%
S3-1	6.60	0.840	99.99%
S3-2	6.97	0.840	99.99%
S3-3	11.71	0.822	99.99%

Next a function to describe the shape parameters EI, FI, and η was constructed. As shown in Figure 14a, the relationship between EI, FI and η was quadratic in nature, described using Eq. (13). Referring to Eq. (12), τ_p can be further expressed using Eq. (14). In particular, when $EI = 1.00$ and $FI = 0.839$, the minima value ($\eta_{\min}$) was 4.26. Fig. 14b showed the peak shear strength distribution

fitted using Eq. (14) at σ_n=100 kPa, where the minimum value $\tau_{\mathrm{p\,min}}$ was 194.63kPa.

$$\eta(EI, FI) = 46.54 - 34.09EI - 60.92FI + 13.79EI^2 + 31.12FI^2 + 8.61EIFI \quad (13)$$

$$\tau_p = \eta(EI, FI)\sigma_n{}^{\beta} \quad (14)$$

On the other hand, Figure 14b showed that there were some differences in the effects of EI and FI on the shear strength of the coarse aggregates. For instance, the oblate-equant specimen had a τ_p value of 232.60 kPa, while prolate-equant specimen had a τ_p value of 208.06 kPa, (a difference of 10.55%). Similarly, the oblate specimen had a τ_p value of 305.91 kPa, while τ_p for the oblate specimen had a value of 318.43 kPa, (a difference of 4.09%). However, compared to the differences in τ_p for specimens with different aspect ratios, the effect of P_2 in particle was relatively low. The compacted state of the coarse aggregates or analytical bias resulting from the sample number could explain this finding.

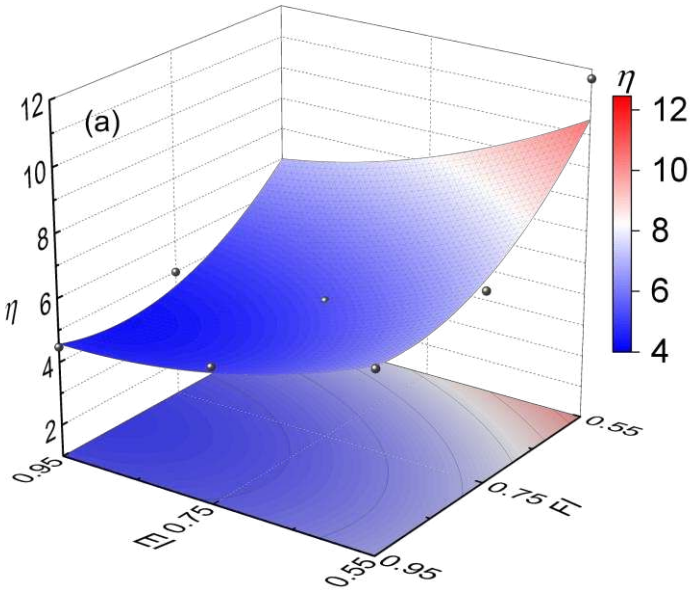

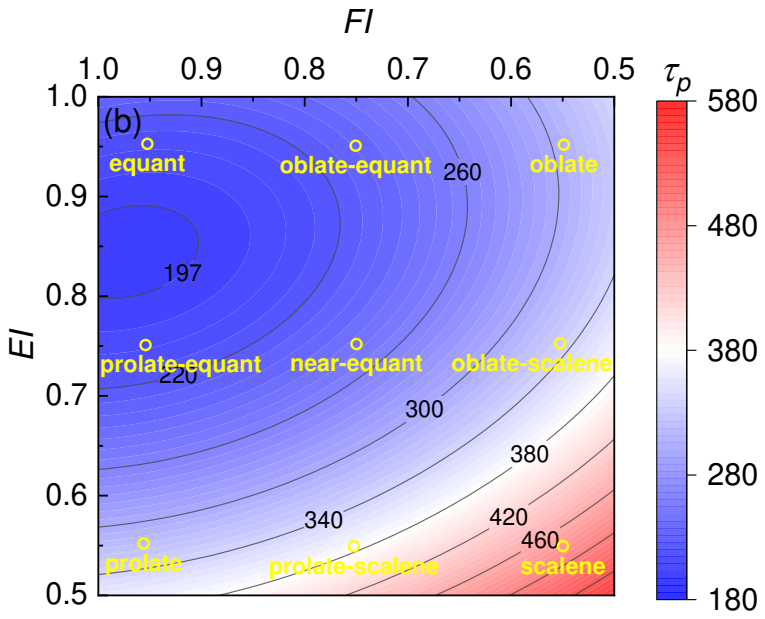

Fig. 14. Regression coefficients η and τ_p as a function of EI and FI: (a) η (b) τ_p when $\sigma_n =$ 100 kPa.

6.2 Contact force

Particle-particle contacts in granular materials transmit external loads from one boundary to another. These contact forces are a critical factor in determining the mechanical properties of granular materials (Radjai et al., 1998). Inhomogeneity in the spatial distribution of granular materials makes it challenging to characterize their contact networks (Majmudar and Behringer, 2005). Previous investigations (Azéma et al., 2009; Thornton, 2000) show the normal contact force contributes more towards the deviatoric stress tensor than the tangential contact force. Therefore, the purpose of this section is to provide a quantitative analysis of contact force networks based on the normal contact force.

The spatial distribution of normal contact forces can be visualized intuitively using a spherical histogram in which each bar represents the local average normal contact force $\overline{f_n}$ in that direction. The local average normal contact force $\overline{f_n}$ denotes the average of the magnitudes of normal contact forces that fall in the direction intervals of the corresponding bar. The spherical histogram is an exact sphere for an isotropic distribution of normal contact forces. A non-spherical histogram implies an anisotropic distribution of normal contact forces. All specimens exhibit similar shear strength at the

438 same σ_n. Hence, the results were analyzed at σ_n=100 kPa.

439 Figure 15 shows the normal contact force histogram for specimens at different shear displacements
440 ($S = 0, 40, 80$ mm) where the corresponding local minimum average contact force $\bar{f}_{n,min}$ and local
441 maximum average contact force $\bar{f}_{n,max}$ are calculated. At the initial stage of the shear process ($S =$
442 0 mm), the distribution of the corresponding normal contact forces was approximately the same for
443 each specimen, with $\bar{f}_{n,min}$ and $\bar{f}_{n,max}$ ranging from 20 N to 50 N. As shear displacement developed,
444 each specimen gradually exhibited a horizontal distribution of normal contact forces, and the difference
445 between $\bar{f}_{n,min}$ and $\bar{f}_{n,max}$ became larger.

446 The specimens (prolate-equant, oblate-equant, near-equant) increased the aggregate matrix shear
447 strength without changing the internal contact forces compared to those with equant characteristics.
448 Increasing the particle shape's prolate, oblate, or scalene characteristics significantly increased the
449 internal contact forces, despite increased macroscopic shear strength. For instance, given S = 80 mm,
450 $\bar{f}_{n,max}$ of these specimens increased between 2 to 4 times compared to specimens with equant
451 characteristics.

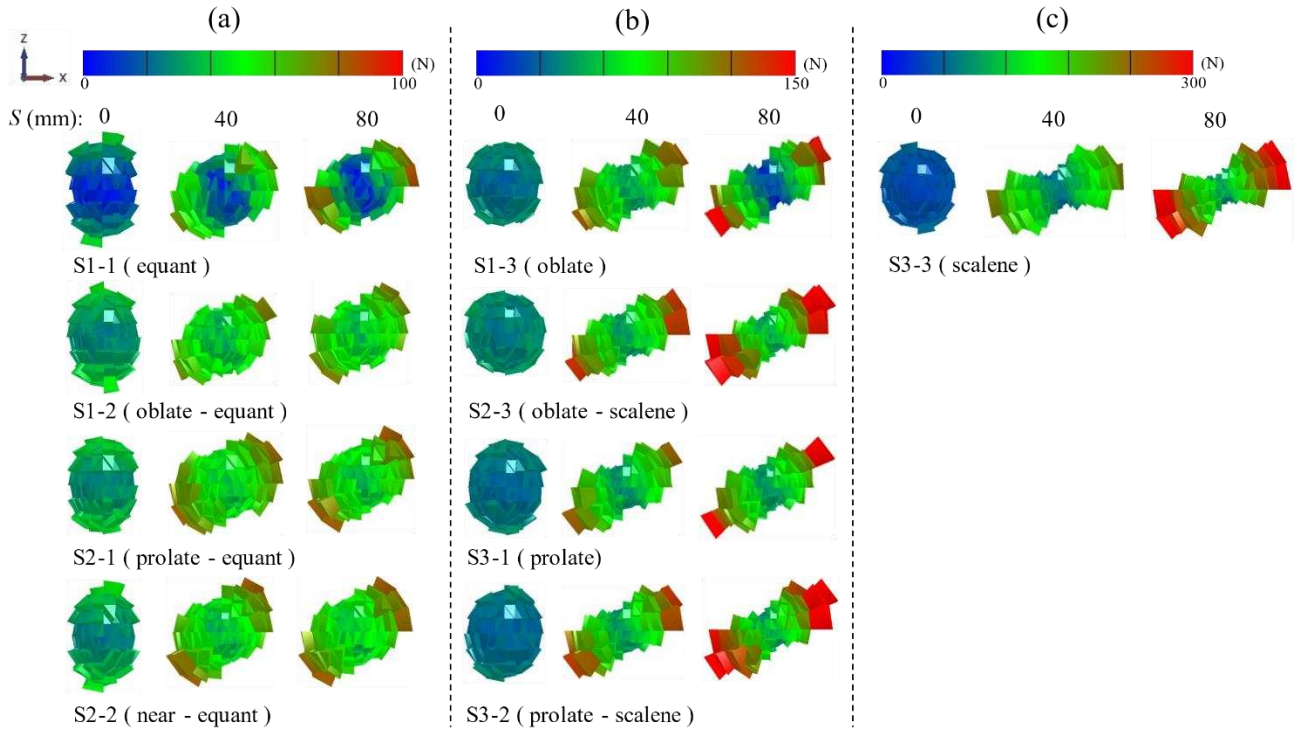

452

Fig. 15. Histogram of normal contact force distribution for coarse aggregates of various shapes: (a) the specimens when *EI* and *FI* ≥ 0.75; (b) the specimens When *EI* ≤ 0.55 or *FI* ≤ 0.55; (c) the specimens when *EI* and *FI* ≤ 0.55.

6.3 Fabric tensor

Fabric anisotropy is an important characteristic of granular materials. Therefore, the concept of a fabric tensor (Oda, 1982; Satake, 1978) is now studied to investigate the internal structure of aggregates. According to (Oda, 1982; Ouadfel and Rothenburg, 2001), the probability density function $E_{(c)}$ of contact normals (the unit normal vector between contact particles) at a spherical unit surface is:

$$\int_0^{2\pi}\int_0^{\pi} E_{(c)}\, sin(\beta)\, d\alpha d\beta = 1 \tag{15}$$

where the ranges of α and β are $0 \leq \alpha < 2\pi$ and $0 \leq \beta < \pi$, respectively. Hence, the fabric tensor of a contact normal can be expressed as:

$$\Phi_{ij} = \int_0^{2\pi}\int_0^{\pi} E_{(c)}\, n_i\, n_j sin(\beta)\, d\alpha d\beta \tag{16}$$

where n_i is the unit vector of a contact normal, given as a column vector $(\sin(\beta)\cos(\alpha), \sin(\beta)\sin(\alpha), \cos(\beta))$; n_j is the transpose matrix of n_i, which can also be written as n_i^T. The corresponding fabric tensor can be readily obtained from DEM results as:

$$\Phi_{ij} = \frac{1}{N_c}\sum_{k=1}^{N_c} n_i n_j \tag{17}$$

where N_c denotes the total number of contacts in the granular assembly, and $i, j = x, y, z$ in the Cartesian coordinate system.

The fabric tensor in Eq. (17) has three eigenvalues, Φ_1, Φ_2, Φ_3 ($\Phi_1 \geq \Phi_2 \geq \Phi_3$) and three corresponding eigenvectors. The eigenvectors and eigenvalues determine the direction and size of fabric anisotropy respectively. A deviatoric eigenvalue (Barreto et al., 2009) was proposed to determine the anisotropy under the influence of three eigenvalues of the fabric tensor. Note that fabric tensors

exhibit greater anisotropy with increasing deviatoric eigenvalues. Deviatoric eigenvalues indicate the concentration of embedded forces that resist shear deformation. The concentration of embedded forces increase the contact forces on the particles in the shear region, resulting in particle fragmentation. Following the concept above, Φ_d reflected the anisotropy of the fabric tensor (deviatoric fabric tensor), expressed by:

$$\Phi_d = \frac{1}{\sqrt{2}}\sqrt{(\Phi_1 - \Phi_2)^2 + (\Phi_1 - \Phi_3)^2 + (\Phi_2 - \Phi_3)^2} \quad (18)$$

Figure 16 shows the variation of Φ_d with S for different specimens at σ_n=100 kPa. Φ_d increased with increasing S for all specimens, and the trend in Φ_d differed from specimen to specimen.

Given $\sigma_n = 100$ kPa and $S = 80$ mm, a quadratic function was used to establish the relationship between EI, FI and Φ_d, as shown in Figure17a and Eq. (19). $\Phi_{d\,min}$=0.026 when $EI = 0.856$ and $FI = 0.849$.

$$\Phi_d(EI, FI) = 0.84 - 1.00EI - 0.91FI + 0.48EI^2 + 0.43FI^2 + 0.21EIFI \quad (19)$$

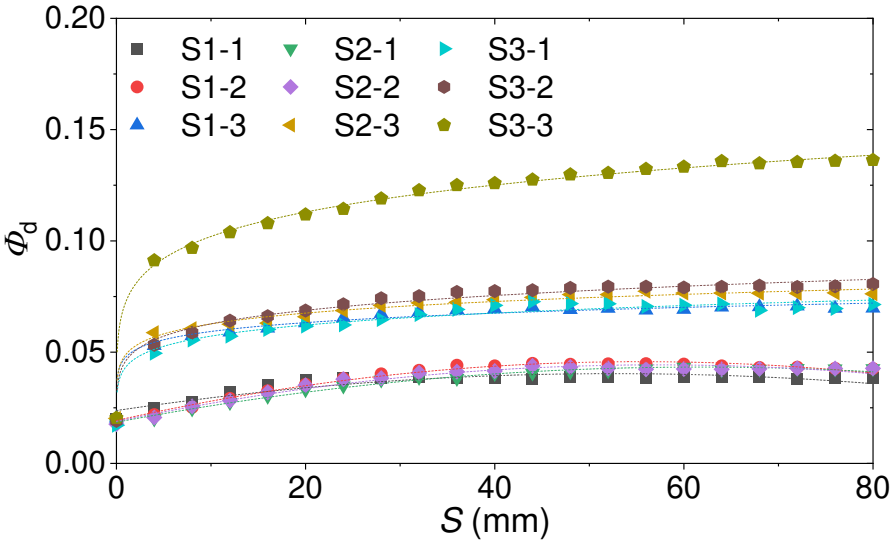

Fig. 16. Variation in Φ_d with S at $\sigma_n = 100$ kPa.

Figure 17b demonstrates that EI and FI had approximately equal influences on Φ_d for coarse aggregates. For instance, Φ_d was 0.032 for oblate-equant specimens and 0.033 for prolate-equant specimens, a difference of 3.13%. Φ_d was 0.063 for oblate specimens and 0.069 for prolate specimens, a difference of 9.60%. Φ_d was 0.076 for oblate-scalene specimens, and 0.081 for prolate-

scalene specimen, a difference of 6.56%. All the above cases show that the influence of EI and FI on Φ_d for coarse aggregates was similar. The intermediate axis P_2 of particles could be ignored due to its limited influence.

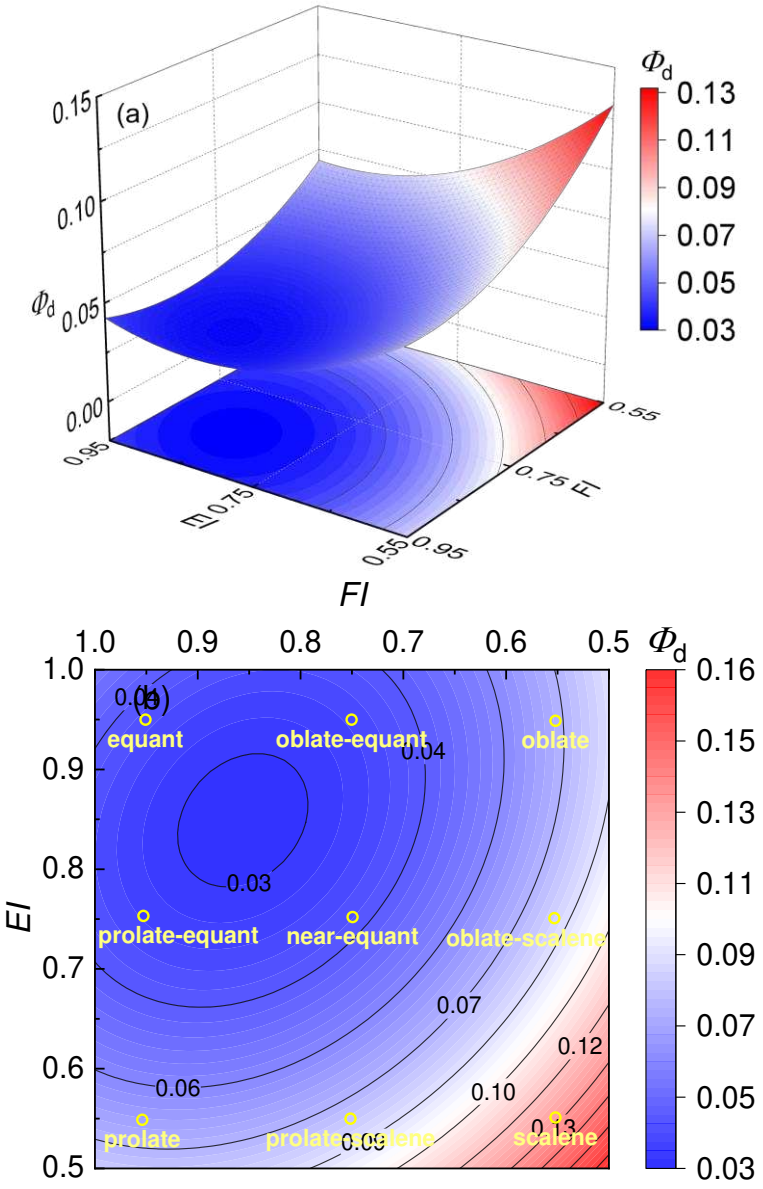

Fig. 17. Φ_d as a function of EI and FI at $\sigma_n = 100$ kPa and $S = 20\%$: (a) fitted quadratic surface; (b) contour.

It should be emphasized that the preceding analysis assumed that particles were not subject to fragmentation. The results show that as particle irregularity becomes more significant, shear strength of the assemblies increases, which contradicts certain experimental findings (Jing et al., 2020). Indeed, more irregular particle shapes can lead to increased bending moments and a higher likelihood of

505 fragmentation (Afshar et al., 2017; Fang et al., 2022; Zou, 2018). The utilization of non-crushable
506 particles in DEM simulations has inherent limitations since it may diverge from actual scenarios once
507 particle breakage ensues. Nevertheless, the use of rigid blocks presents an advantageous technique for
508 scrutinizing inter-particle contact conditions, independent of the particle strength. Consequently, it is
509 possible to identify aspect ratio thresholds as a benchmark for selecting suitable particle shapes that
510 mitigate grain crushing while providing adequate strength for the fabrication of aggregate supporting
511 layers in transportation infrastructure.

512 Similar to the analysis approach in Section 5.2, the influence of *FEI* on Φ_d was analyzed. Based
513 on the grain irregularity, the relative deviatoric fabric tensor Φ_{r} is defined as:

514 $$\Phi_{\mathrm{r}} = \frac{\Phi_{\mathrm{d\,max}} - \Phi_{\mathrm{d}}}{\Phi_{\mathrm{d\,max}} - \Phi_{\mathrm{d\,min}}} \tag{20}$$

515 where $\Phi_{\mathrm{d\,min}}$ is the minimum value calculated by Eq. (19) and $\Phi_{\mathrm{d\,max}}$ occurs when the specimen
516 is scalene.

517 As shown in Fig.18 and Eq. (21), there is an exponential relationship between FEI and Φ_{r}. The
518 fitted data were obtained from simulations based on the particle samples in Section 5.2. As FEI
519 increased, Φ_{r} first increased rapidly and then slowly. The maximum curvature of this function was
520 taken as the threshold for the variation in Φ_{r} with FEI. The maximum value of curvature existed
521 when $FEI = 0.47$.

522 $$\Phi_{\mathrm{r}} = 0.88 - 19.71e^{-10FEI} \tag{21}$$

523 Thus, when there is an axial particle size difference, for example if the aggregates have prolate,
524 oblate, or scalene shapes, the anisotropy of the fabric tensor increases dramatically. It is possible to
525 minimise the potential for particle breakage by maintaining *FEI* greater than the threshold (0.47).
526 Accordingly, the ratio of the maximum and minimum axial dimensions, can be considered to be
527 approximately 2:1.

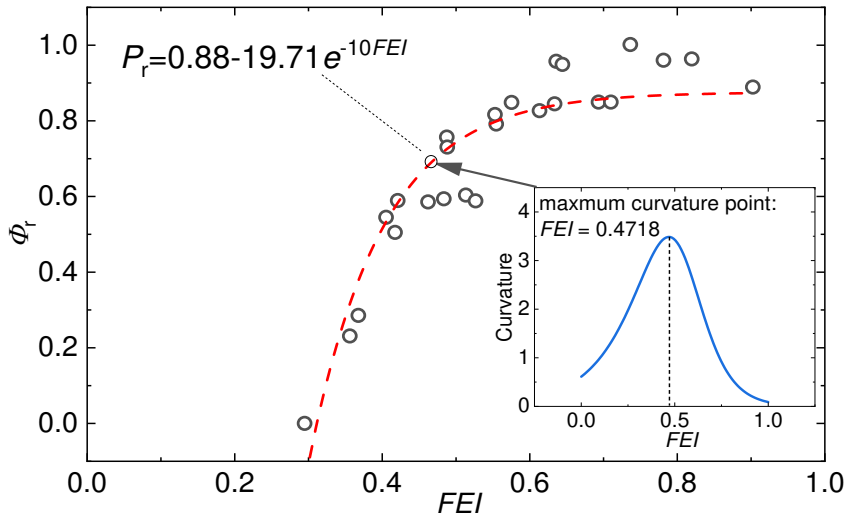

Fig. 18. Variation in Φ_r with FEI and the corresponding curvature distribution ($\sigma_n = 100$ kPa, $S = 80$ mm).

7 Conclusions

A quantitative investigation was carried out to examine the impact of particle aspect ratio on the compaction characteristics and shear behavior of coarse aggregates. The study employed laser scanning technology to obtain 3D surface profiles of 700 coarse aggregate particles, from which three orthogonal axial dimensions (P_1, P_2, P_3), *EI*, *FI*, and *FEI* indexes were selected to characterize particle shapes. To simulate the compaction and direct shear tests on nine typical coarse aggregates with representative shapes, DEM simulations were employed. Mathematical functions were developed from macro- and meso-scale perspectives to relate shape indexes to porosity, shear strength, and the fabric tensor. The major conclusions are:

a) Regarding the *EI* and *FI* indexes, statistical indicators such as the fitting parameters of Weibull distribution, mean, coefficient of variation, skewness, and kurtosis show no significant difference between the real particles and the reproduced Rblocks. It is evident that Rblocks are capable of effectively depicting the actual shape of coarse aggregates in discrete element simulations.

b) In regards to compaction, an exponential function characterizes the correlation between the inter-particle friction and porosity, whereas the regression parameter ζ can be defined as a quadratic function of *EI* and *FI*. The impact of *EI* and *FI* on particle porosity is analogous. A threshold of $FEI \approx$

0.5 can regulate the packing density of coarse aggregates.

c) The relationship between the peak shear strength and vertical stress with the same initial porosity can be described by a power function. The regression parameter η can be expressed as a quadratic function of *EI* and *FI*. The effect of *EI* and *FI* on the peak shear strength of the assemblies is similar.

d) Distinct aggregate shapes result in varying distributions of normal contact forces. Prolate or oblate particles, in particular, exhibit a noteworthy increase in the inhomogeneity of the normal contact force distribution. The anisotropy of the fabric tensor is influenced similarly by both *EI* and *FI*. The relative anisotropy of the fabric tensor can be utilized as a guide to choose appropriate aspect ratios while maintaining control over particle fragmentation.

The novel equations that were developed can aptly represent the correlation between the aspect ratios and the compaction/shear properties. By using the proposed *FEI* threshold, which is based on the relative porosity and the relative anisotropy of the fabric tensor, suitable coarse aggregates can be selected for use as fill material.

Acknowledgements

This work was supported by the National Natural Science Foundation of China (grant number 52078435), the Royal Society (grant number IEC\NSFC\211306 - International Exchanges 2021 Cost Share), the Natural Science Foundation of Sichuan Province (grant numbers 2023NSFSC0391 and 2022NSFSC0404), and the 111 Project (grant number B21011).

References

Abbireddy, C., Clayton, C., 2010. Varying initial void ratios for DEM simulations. Geotechnique 60, 497–502.

Afshar, T., Disfani, M.M., Arulrajah, A., Narsilio, G.A., Emam, S., 2017. Impact of particle shape on breakage of recycled construction and demolition aggregates. Powder Technol. 308, 1–12.

American Society of Testing and Materials, 2010. Standard test method for flat particles, elongated particles, or flat and elongated particles in coarse aggregate (D4791-2010). ASTM International, West Conshohocken.

572 Australian Standard, 2007. Methods for sampling and testing aggregates-method 14: particle shape, by proportional
573 caliper (AS 1141.14-2007). Standards Australia Ltd, Sydney.
574 Azéma, E., Radjaï, F., 2010. Stress-strain behavior and geometrical properties of packings of elongated particles.
575 Phys. Rev. E 81, 051304.
576 Azéma, E., Radjai, F., Saussine, G., 2009. Quasistatic rheology, force transmission and fabric properties of a packing
577 of irregular polyhedral particles. Mech. Mater. 41, 729–741.
578 Barreto, D., O'Sullivan, C., Zdravkovic, L., 2009. Quantifying the evolution of soil fabric under different stress paths.
579 Presented at the AIP Conference Proceedings, American Institute of Physics, pp. 181–184.
580 Barrett, P., 1980. The shape of rock particles, a critical review. Sedimentology 27, 291–303.
581 Bian, X., Li, W., Li, G., 2015. Three-dimensional discrete element analysis of railway ballast's shear process based
582 on particles's real geometry. Eng. Mech. 32, 64–75.
583 Bono, D., McDowell, G., Wanatowski, D., 2014. DEM of triaxial tests on crushable cemented sand. Granul. Matter
584 16, 563.
585 Bowman, E.T., Soga, K., Drummond, W., 2001. Particle shape characterisation using Fourier descriptor analysis.
586 Geotechnique 51, 545–554.
587 Cheng, Z., Wang, J., 2018. Experimental investigation of inter-particle contact evolution of sheared granular materials
588 using X-ray micro-tomography. Soils Found. 58, 1492–1510.
589 Cho, G., Dodds, J., Santamarina, C., 2006. Particle shape effects on packing density, stiffness, and strength: natural
590 and crushed sands. J Geotech Geoenviron 132 (5): 591–602.
591 Cook, C.S., Tanyu, B.F., Yavuz, A.B., 2017. Effect of particle shape on durability and performance of unbound
592 aggregate base. J. Mater. Civ. Eng. 29, 04016221.
593 Cundall, P.A., Strack, O.D., 1979. A discrete numerical model for granular assemblies. geotechnique 29, 47–65.
594 Dai, B.B., Yang, J., Zhou, C.Y., 2016. Observed effects of interparticle friction and particle size on shear behavior of
595 granular materials. Int. J. Geomech. 16, 04015011.
596 Donev, A., Cisse, I., Sachs, D., Variano, E.A., Stillinger, F.H., Connelly, R., Torquato, S., Chaikin, P.M., 2004.
597 Improving the density of jammed disordered packings using ellipsoids. Science 303, 990–993.
598 Donev, A., Torquato, S., Stillinger, F.H., 2005a. Neighbor list collision-driven molecular dynamics simulation for
599 nonspherical hard particles. I. Algorithmic details. J. Comput. Phys. 202, 737–764.
600 Donev, A., Torquato, S., Stillinger, F.H., 2005b. Neighbor list collision-driven molecular dynamics simulation for
601 nonspherical hard particles.: II. applications to ellipses and ellipsoids. J. Comput. Phys. 202, 765–793.
602 Fang, C., Gong, J., Jia, M., Nie, Z., Li, B., Mohammed, A., 2022. Investigating the effects of elongation and flatness
603 on the shear behaviour of breakable granular materials via the DEM. Granul. Matter 24, 1–23.
604 Ferellec, J., McDowell, G., 2010. Modelling realistic shape and particle inertia in DEM. Géotechnique 60, 227–232.
605 Fraige, F.Y., Langston, P.A., Matchett, A.J., Dodds, J., 2008. Vibration induced flow in hoppers: DEM 2D polygon
606 model. Particuology 6, 455–466.
607 Fu, L., Zheng, Y., Tian, Z., Huang, S., Zhou, S., 2022. Importance of examining particle movements in modelling
608 ballast bed via discrete element method. Int. J. Rail Transp. 10, 547–561.
609 Garboczi, E., 2011. Three dimensional shape analysis of JSC-1A simulated lunar regolith particles. Powder Technol.
610 207, 96–103.
611 Gilbert, E.G., Johnson, D.W., Keerthi, S.S., 1988. A fast procedure for computing the distance between complex
612 objects in three-dimensional space. IEEE J. Robot. Autom. 4, 193–203.
613 Gong, J., Nie, Z., Zhu, Y., Liang, Z., Wang, X., 2019. Exploring the effects of particle shape and content of fines on
614 the shear behavior of sand-fines mixtures via the DEM. Comput. Geotech. 106, 161–176.
615 Guo, Y., Xie, J., Fan, Z., Markine, V., Connolly, D.P., Jing, G., 2022. Railway ballast material selection and evaluation:

A review. Constr. Build. Mater. 344, 128218.
Huang, Q., Zhan, M., Sheng, J., Luo, Y., Zhang, X., 2015. Numerical method to generate granular assembly with any desired relative density based on DEM. Chin. J. Geotech. Eng. 37, 537–543.
Itasca Consulting Group, 2017. PFC 6.0 Documentation. Minneapolis, Minnesota.
Jing, G., Qiang, W., Chang, J., Li, X., 2020. Effect of flakiness-elongation index on shear behaviour of railway ballast. Jounal Southwest Jiaotong Univ. 55, 688–694.
Kuhn, M.R., Sun, W., Wang, Q., 2015. Stress-induced anisotropy in granular materials: fabric, stiffness, and permeability. Acta Geotech. 10, 399–419.
Lee, C., Suh, H.S., Yoon, B., Yun, T.S., 2017. Particle shape effect on thermal conductivity and shear wave velocity in sands. Acta Geotech. 12, 615–625.
Li, C., Xu, W., Meng, Q., 2015. Multi-sphere approximation of real particles for DEM simulation based on a modified greedy heuristic algorithm. Powder Technol. 286, 478–487.
Lin, X., Ng, T., 1995. Contact detection algorithms for three-dimensional ellipsoids in discrete element modelling. Int. J. Numer. Anal. Methods Geomech. 19, 653–659.
Lu, R., Luo, Q., Wang, T., Zhao, C., 2022. Comparison of clumps and rigid blocks in three-dimensional DEM simulations: curvature-based shape characterization. Comput. Geotech. 151, 104991.
Majmudar, T.S., Behringer, R.P., 2005. Contact force measurements and stress-induced anisotropy in granular materials. nature 435, 1079–1082.
Mitchell, J.K., Soga, K., 2005. Fundamentals of soil behavior. John Wiley & Sons New York.
Mollon, G., Zhao, J., 2014. 3D generation of realistic granular samples based on random fields theory and Fourier shape descriptors. Comput. Methods Appl. Mech. Eng. 279, 46–65.
National Railway Administration of PRC, 2017. Code for design of railway earth structure (TB10001-2016). China Railway Publishing House, Beijing.
National Railway Administration of PRC, 2010. Code for soil test of railway engineering (TB10102-2010). China Railway Publishing House, Beijing.
National Railway Administration of PRC, 2008. Railway ballast (TB/T 2140-2008). China Railway Publishing House, Beijing.
Ng, T., 2009. Particle shape effect on macro-and micro-behaviors of monodisperse ellipsoids. Int. J. Numer. Anal. Methods Geomech. 33, 511–527.
Ngo, T., Indraratna, B., 2020. Analysis of deformation and degradation of fouled ballast: Experimental testing and DEM modeling. Int. J. Geomech. 20, 06020020.
Nie, J.-Y., Cao, Z.-J., Li, D.-Q., Cui, Y.-F., 2021. 3D DEM insights into the effect of particle overall regularity on macro and micro mechanical behaviours of dense sands. Comput. Geotech. 132, 103965.
Nie, Z., Fang, C., Gong, J., Liang, Z., 2020. DEM study on the effect of roundness on the shear behaviour of granular materials. Comput. Geotech. 121, 103457.
Oda, M., 1982. Fabric tensor for discontinuous geological materials. Soils Found. 22, 96–108.
Ouadfel, H., Rothenburg, L., 2001. Stress–force–fabric'relationship for assemblies of ellipsoids. Mech. Mater. 33, 201–221.
Payan, M., Senetakis, K., Khoshghalb, A., Khalili, N., 2017. Effect of gradation and particle shape on small-strain Young's modulus and Poisson's ratio of sands. Int. J. Geomech. 17, 04016120.
Radjai, F., Wolf, D.E., Jean, M., Moreau, J.-J., 1998. Bimodal character of stress transmission in granular packings. Phys. Rev. Lett. 80, 61.
Rajan, B., Singh, D., 2017. Comparison of shape parameters and laboratory performance of coarse aggregates produced from different types of crushing operations. J. Mater. Civ. Eng. 29, 04017044.

Rothenburg, L., Bathurst, R., 1992. Micromechanical features of granular assemblies with planar elliptical particles. Geotechnique 42, 79–95.
Satake, M., 1978. Constitution of mechanics of granular materials through graph representation. Theor. Appl. Mech. 26, 257–266.
Shin, H., Santamarina, J.C., 2013. Role of particle angularity on the mechanical behavior of granular mixtures. J. Geotech. Geoenvironmental Eng. 139, 353–355.
Su, D., Yan, W., 2018. 3D characterization of general-shape sand particles using microfocus X-ray computed tomography and spherical harmonic functions, and particle regeneration using multivariate random vector. Powder Technol. 323, 8–23.
Thornton, C., 2000. Numerical simulations of deviatoric shear deformation of granular media. Géotechnique 50, 43–53.
Wadell, H., 1935. Volume, shape, and roundness of quartz particles. J. Geol. 43, 250–280.
Wu, M., Xiong, L., Wang, J., 2021. DEM study on effect of particle roundness on biaxial shearing of sand. Undergr. Space 6, 678–694.
Xiao, J., Zhang, X., Zhang, D., Xue, L., Sun, S., Stránský, J., Wang, Y., 2020. Morphological reconstruction method of irregular shaped ballast particles and application in numerical simulation of ballasted track. Transp. Geotech. 24, 100374.
Xiao, Y., Tutumluer, E., 2017. Gradation and packing characteristics affecting stability of granular materials: aggregate imaging-based discrete element modeling approach. Int. J. Geomech. 17, 04016064.
Xu, W., Wang, S., 2016. Meso-mechanics of soil-rock mixture with real shape of rock blocks based on 3D numerical direct shear test. Chin. J. Rock Mech. Eng. 35, 2152–2160.
Zhang, T., Zhang, C., Zou, J., Wang, B., Song, F., Yang, W., 2020. DEM exploration of the effect of particle shape on particle breakage in granular assemblies. Comput. Geotech. 122, 103542.
Zhang, X., 2017. Numerical simulation and experiment study on macro-meso mechanical behaviours of high-speed railway ballast. Southwest Jiaotong University.
Zhao, B., Wang, J., 2016. 3D quantitative shape analysis on form, roundness, and compactness with μCT. Powder Technol. 291, 262–275.
Zhao, L., Zhang, S., Huang, D., Wang, X., Zhang, Y., 2020. 3D shape quantification and random packing simulation of rock aggregates using photogrammetry-based reconstruction and discrete element method. Constr. Build. Mater. 262, 119986.
Zhao, S., Zhou, X., 2017. Effects of particle asphericity on the macro-and micro-mechanical behaviors of granular assemblies. Granul. Matter 19, 1–18.
Zheng, J., Hryciw, R.D., 2016. A corner preserving algorithm for realistic DEM soil particle generation. Granul. Matter 18, 1–18.
Zhou, B., Wang, J., 2017. Generation of a realistic 3D sand assembly using X-ray micro-computed tomography and spherical harmonic-based principal component analysis. Int. J. Numer. Anal. Methods Geomech. 41, 93–109.
Zhou, B., Wang, J., Zhao, B., 2015. Micromorphology characterization and reconstruction of sand particles using micro X-ray tomography and spherical harmonics. Eng. Geol. 184, 126–137.
Zhou, G.G., Sun, Q., 2013. Three-dimensional numerical study on flow regimes of dry granular flows by DEM. Powder Technol. 239, 115–127.
Zingg, T., 1935. Beitrag zur schotteranalyse. ETH Zurich.
Zou, D., 2018. Three-dimensional shape of rockfill material and its influence on particle breakage. Rock Soil Mech. 39, 3525–3530.

704